On the Supercapacitive Behaviour of Anodic Porous WO$_3$-Based Negative Electrodes

Kush K. Upadhyay[a,1,*], Marco Altomare[b,1,*], Sonia Eugénio[a], Patrik Schmuki[b,c], Teresa M. Silva[a,d], Maria Fàtima Montemor[a]

[a] CQE, Instituto Superior Técnico, Universidade de Lisboa, Av. Rovisco Pais, 1049-001 Lisboa, Portugal
[b] Department of Materials Science, Institute for Surface Science and Corrosion WW4-LKO, University of Erlangen-Nuremberg, Martensstraße 7, D-91058 Erlangen, Germany
[c] Chemistry Department, Faculty of Sciences, King Abdulaziz University, 80203 Jeddah, Saudi Arabia
[d] Department of Mechanical Engineering, GI-MOSM, Instituto Superior de Engenharia de Lisboa-ISEL, 1950-062 Lisboa, Portugal

ARTICLE INFO

ABSTRACT

Herein we illustrate the functionality as pseudocapacitive material of tungsten trioxide (WO$_3$) nanochannel layers fabricated by electrochemical anodization of W metal in pure hot ortho-phosphoric acid (o-H$_3$PO$_4$). These layers are characterized by a defined nanochannel morphology and show remarkable pseudocapacitive behaviour in the negative potential (-0.8–0.5 V) in neutral aqueous electrolyte (1 M Na$_2$SO$_4$). The *maximum* volumetric capacitance of 397 F cm^{-3} is obtained at 2 A cm^{-3}. The WO$_3$ nanochannel layers display full capacitance retention (up to 114%) after 3500 charge-discharge cycles performed at 10 A cm^{-3}. The relatively high capacitance and retention ability are attributed to the high surface area provided by the regular and defined nanochannel morphology. Kinetic analysis of the electrochemical results for the best performing WO$_3$ structures, *i.e.*, grown by 2 h-long anodization, reveals the occurrence of pseudocapacitance and diffusional controlled processes. Electrochemical impedance spectroscopy measurements show for the same structures a relatively low electrical resistance, which is the plausible cause for the superior electrochemical behaviour compared to the other structures.

© 2017 Elsevier Ltd. All rights reserved.

1. Introduction

Energy, environment and health are regarded as biggest challenges in the modern world. Owing to the steeply increased demand of energy *per capita* and consequent environmental pollution, conversion, storage and efficient management of renewable energy have become world-wide subjects of intense scientific research. Considerable efforts have been made to develop efficient, green, and renewable energy-related technologies, based on the use of *e.g.* supercapacitors, lithium-ion batteries, solar cells, fuel cells, and photocatalytic and photothermal conversion processes [1–5].

In the context of energy storage, supercapacitors (also known as electrochemical capacitors or ultracapacitors) are currently attracting wide attention. Remarkable characteristics, such as their high power density, fast charge/discharge rates and long cycle lifetime, bridge the gap between high-specific energy batteries and high-specific power conventional capacitors [6–9].

Presently, the most important developments in this field entail the use of novel active electrode materials to further enhance the overall energy density of the supercapacitors − the goal is to fulfil the energy requirement at various scales, ranging from simple and low-consumption electronic devices to electric driven vehicles.

In order to accomplish the desired energy density, a primary strategy is to increase the working potential window of the supercapacitor. This result can be achieved by using organic- or ionic liquid-based electrolytes, which enable potential windows of up to 3 V [10]. However, organics present activity only towards a small group of electrode materials, namely carbon-based materials, while ionic liquids are still expensive to be envisaged as a

---

practical solution. Additionally, these electrolytes have some other drawbacks, such as a decreased ionic conductivity, high toxicity, flammability, and safety issues which severely restricts their applicability [10].

In this frame, a promising approach is to assemble asymmetric systems, using aqueous electrolytes, in which different electrode materials (having different active potential windows) can be combined, resulting in the advantageous widening of the working potential window of the device [11].

Most of the research performed to date on the development of electrode materials for asymmetric supercapacitors has focused on electrode materials working in positive potential region. On the other hand, the exploration of redox-responsive negative electrode materials is still relatively new, so that generally the negative electrodes do not fulfil the demands of high energy density [10].

In the quest for more efficient negative electrode materials, high-surface area carbon based materials are being explored [12]. Although they deliver excellent power density, carbon based materials do not fulfil requirements in terms of energy density, which is a serious limitation.

The use of pseudocapacitive materials, such as transition metal oxides and conducting polymers [12–15], instead of carbon based materials, leads to enhanced energy density without significant loss of power density. This enhancement results from the additive effect of fast superficial redox reactions and electric double layer formation at the electrode/electrolyte interface. Transition metal oxides such as Fe_2O_3, MoO_3, Mn_3O_4, and WO_3 [12,16–23] show promising pseudocapacitive behaviour as well as reasonable capacity retention in asymmetric systems in the negative potential region.

Among them, tungsten oxide (WO_x, $x \leq 3$) is currently receiving considerable attention, not only in light of its chemical stability and good electrical conductivity but also due to its widely tuneable composition [24–26]. Particularly, WO_3 materials show efficient charge storage/delivery dynamic owing to the reversible valence change, *i.e.*, change of oxidation state between W^{6+} and W^{5+} centres [24–27]. Due to this reversible change, WO_x derived materials are also widely used as electrode for electrochromic devices [24–27]).

The morphology of the material also plays an important role, *i.e.*, a large surface area of the electrode is key factor towards improved specific capacitance [28,29]. In this regard, one dimensional (1D) nanostructured materials (such as nanorods, nanotubes, nanochannels *etc.*) are advantageous because they offer large specific surface area, 1D charge transport pathway, and can also withstand volume changes (expansion) allowing strain accommodation during intercalation/deintercalation processes [30–32].

Among different nanostructuring techniques, electrochemical anodization has gained large attention in the last decades for fabricating nanopore, nanochannel and nanotube layers of various metal oxides [33–37]. This simple approach is based on the anodization of a metal piece in a suitable electrolyte–the result is that under adequate (*i.e.*, self-organizing) electrochemical conditions highly-ordered vertically-aligned arrays of 1D metal oxide nanostructures can be grown on the (conductive) metal substrate.

Key advantage of this approach is that the morphology of the nanostructures can be finely adjusted by simple electrochemical parameters (*e.g.*, applied voltage, electrolyte composition, anodization time, *etc.*) [38,39]. Moreover, these 1D oxide layers are already well back-contacted and are hence ready to be used *e.g.* for electrochemical applications. On the contrary, powders of WO_3 nanostructures fabricated by various approaches other than electrochemical anodization can be explored in view of their supercapacitive behaviour only in the form of composites, *e.g.*

combined with conductive materials such as polyaniline [40,41], which acts as binder and conductive support.

In this work, we report on the fabrication of 1D anodic WO_3 nanochannel layers and their use (without addition of binder, conductive polymers *etc.*) as negative electrodes for asymmetric supercapacitor. The WO_3 nanochannel layers are formed by self-organizing electrochemical anodization of W metal foils in pure hot o-H_3PO_4 electrolyte [42]. The electrochemical performance of the WO_3 electrodes is explored in relation to the layer thickness. The electrochemical response of the WO_3 electrodes shows a remarkable volumetric capacitance of $397\,F\,cm^{-3}$, measured at $2\,A\,cm^{-3}$ in the -0.8–$0.5\,V$ potential range, along with full capacitance retention after 3500 charge-discharge cycles performed at $10\,A\,cm^{-3}$.

2. Experimental Section

2.1. Material preparation

Self-organized vertically-aligned WO_3 nanochannel layers were fabricated by electrochemical anodization of W metal in pure molten ortho-phosphoric acid [42].

W foils (0.125 mm thick, 99.95% purity, Advent Research Materials LTD, Oxford, UK) were cut into $1.5\,cm \times 1.5\,cm$ pieces, cleaned by ultra-sonication in acetone, ethanol and de-ionized water (10 min each) and finally dried in a N_2 stream.

WO_3 nanochannel layers were grown by anodization using a two-electrode electrochemical cell where the W and Pt foils were used as working and counter electrode, respectively. Prior to anodization, one side of the W foil was coated with Kapton tape (DuPont). The two electrodes were immersed into the molten electrolyte in vertical configuration and placed at a distance of two cm from each other. The uncoated side of the W foil faced the Pt counter electrode, and was immersed into the hot electrolyte in order to form an anodic surface of $\sim 2\,cm^2$ ($\sim 1.5\,cm \times 1.3\,cm$).

The electrolyte was composed of (nominally) pure molten ortho-phosphoric acid (o-H_3PO_4, $\geq 99\%$, Sigma-Aldrich), and was constantly stirred during the anodization experiments and kept at the desired temperature ($\sim 100\,°C$) by thermostatic control provided by a heating-stirring plate that was equipped with a Teflon-lined thermocouple immersed into the anodizing *medium*.

The experiments were performed under potentiostatic conditions applying a constant potential of 5 V (no sweeping) provided by a Volcraft VLP 2403 Pro power supply. The resulting current (density) was recorded by using a Keithley 2100 6 $^1/_2$ Digit multimeter interfaced with a laptop. The anodization experiments lasted 1, 2 and 4 h.

The as-formed anodic oxide layers are typically amorphous and were converted into crystalline (monoclinic) WO_3 by annealing in air at 450 °C for 1 h. The thermal treatment was carried out using a rapid thermal annealer (RTA, Jipelec JetFirst100) with heating/cooling rate set at $30\,°C\,min^{-1}$.

2.2. Physicochemical characterization

A Hitachi field emission scanning electron microscope (FE-SEM S4800, Hitachi) was used for morphological characterization of the samples. The thickness and the morphology of the nanostructured films were assessed by SEM analysis of cross-sectional cuts of the anodic layers.

X-ray diffraction (XRD) patterns were collected using an X'pert Philips PMD diffractometer with a Panalytical X'celerator detector, using graphite-monochromized Cu Kα radiation ($\lambda = 1.54056$ Å).

The chemical composition of the anodic layers was determined by X-ray photoelectron spectroscopy (XPS, PHI 5600, US). XPS spectra were acquired using monochromatic Al X-rays source with

a pass energy of 23.5 eV. The XPS spectra were corrected in relation to the C1 s signal at 284.8 eV.

### 2.3. Electrochemical characterization

The anodic WO_3 nanochannel layers grown on tungsten metal substrates were characterized as working electrodes by cyclic voltammetry (CV) and galvanostatic charge-discharge measurements in a 1 M Na_2SO_4 aqueous solution (a freshly prepared electrolyte was used for every experiment).

All measurements were done in a three-electrode setup in which a platinum foil and a saturated calomel electrode (SCE) were used as counter and reference electrode, respectively. A Voltalab PGZ 100 potentiostat was used for all the measurements. The CV curves were obtained at different scan rates (10–100 mV s^{-1}) in a potential window of -1–0.5 V. The galvanostatic charge-discharge
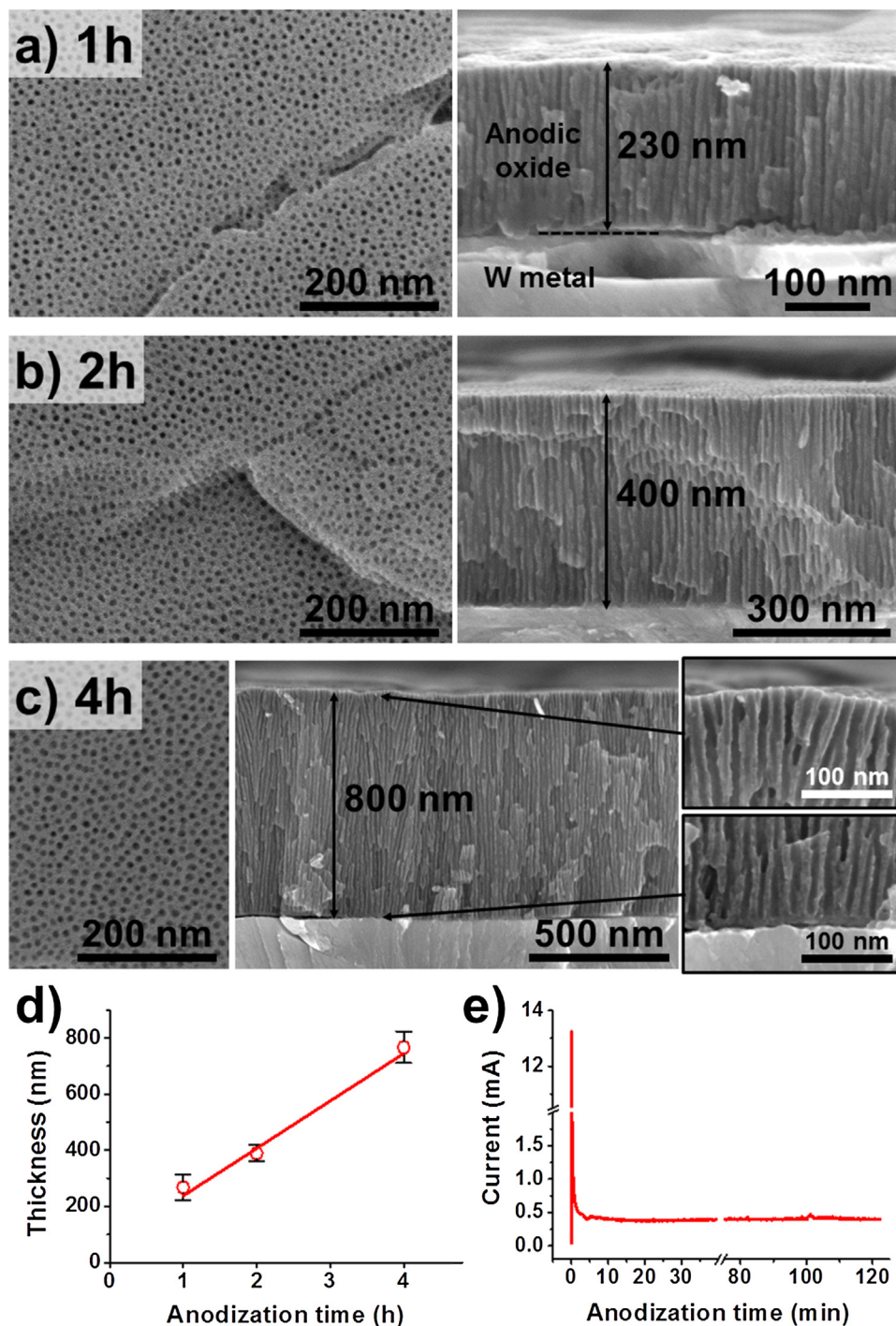
Fig. 1. (a–c) Top-view (left) and cross-sectional (right) SEM images of WO_3 nanochannel layers formed by self-organizing electrochemical anodization of W foils in pure hot o-H_3PO_4 (100 °C -5 V) for different times: (a) 1 h, (b) 2 h and (c) 4 h. (d) Thickness of the WO_3 layers as a function of the anodization time. (e) Typical current $vs.$ time (i-t) profile of a 2 h-long anodization experiment.
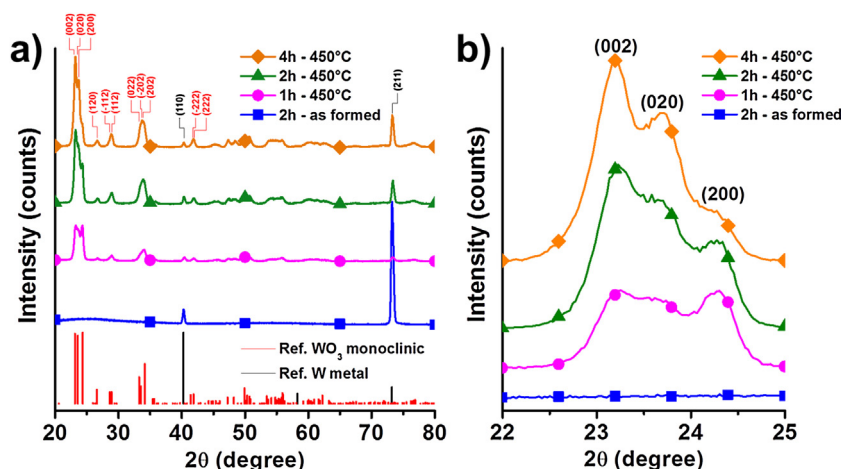
Fig. 2. XRD data: (a) as-formed and annealed (450 °C, 1 h, air) WO$_3$ layers formed on W metal foils by anodizing for different times. The main reflection of monoclinic WO$_3$ and W metal are indexed. The plot also shows references of typical reflection of cubic W metal and monoclinic WO$_3$; (b) plot of the XRD patterns in the 22°–25° 2θ range showing the different relative intensity of the (002), (020) and (200) reflections of monoclinic WO$_3$ for sample grown for different anodization times (1 h, 2 h and 4 h).

profiles were obtained by varying the current density (2–10 A cm^{-3}) in the potential range of −0.8 to 0.5 V.

Electrochemical impedance spectroscopy (EIS) experiments were performed by using a Gamry FAS2 Femtostat, in the frequency range from 0.01 Hz to 10^5 Hz at open circuit potential using 10 mV sinusoidal perturbation.

3. Results and Discussion

Fig. 1a–c show SEM images of typical anodic WO$_3$ nanochannel layers grown in molten o-H$_3$PO$_4$. The use of this electrolyte is a key factor for the growth of ordered WO$_3$ nanochannels as it provides an ideal *equilibrium* between field-assisted passivation of W metal and oxide dissolution [38,43–45], thus establishing the adequate electrochemical conditions for the growth of defined nano-structures. While rapid oxide dissolution that limits the growth of the anodic structure is reported to take place in most common electrolytes [46–48], (nominally) pure hot o-H$_3$PO$_4$ provides an environment with limited water content and with phosphate ions that protect anodic tungsten oxide layer from rapid dissolution [42].

To form WO$_3$ nanochannel electrodes of various thicknesses, anodization experiments were carried out for 1, 2 and 4 h − this resulted in channels with length in the range of ∼200–800 nm. For energy storage, the electrode material mass loading and its conductivity typically determine the device performance [49,50]. The electrochemical performance of the WO$_3$ layers will be thus discussed in relation to their thickness.

The top-view SEM images (Fig. 1a–c, left) show that the top surface of the layers is homogeneous, and that the layers present open pores, with inner diameter of *ca.* 10 nm regardless of the anodization time.

The cross-sectional SEM images (Fig. 1a–c, right) obtained from cross-sectional cuts of the WO$_3$ layers (supported on W foil) show clearly that the anodic WO$_3$ have a nanochannel structure, with aligned vertically-oriented channels that extend from the top surface of the anodic film to the oxide-metal interface. The channels are open at the top surface and remain open (with inner diameter of *ca.* 10 nm) across the entire channel length, regardless of the anodic oxide thickness.

A prolonged anodization time, *i.e.*, from 1 to 2 and 4 h, resulted in a clear increase of the oxide film thickness (Fig. 1d) and the

nanochannel length was found to be of *ca.* 200, 400 and 800 nm, respectively–it is acceptable to assume that the surface area of the nanochannel layers increases with increasing their thickness.

Fig. 1e illustrates a typical current *vs.* time (*i-t*) curve for a WO$_3$ nanochannel layer grown for 2 h. When the anodic potential (5 V) is applied, the recorded current steeply increases and values of current density are reached that are of 6–7 mA cm^{-2}. The current density J is calculated as $J = i/A$, where the recorded current $i \sim 13$ mA and the electrode nominal area $A \sim 2$ cm^2. After the initial peak, the current decreases within a few minutes (∼5 min) and levels off to a steady-state value of ∼0.25 mA cm^{-2}.

The resulting *i-t* behaviour resembles other anodically grown self-organized 1D oxide structures (a most common example is TiO$_2$ nanotube arrays) [45,51]. Here in the first stage of the anodization the W metal substrate develops an initial compact oxide film at the metal/electrolyte interface. After this short stage, an *equilibrium* is established between the metal oxide growth and the field-assisted electrochemical dissolution of the formed oxide. As a result, anodic oxides can grow in the form of vertically-aligned nanochannels [43,44].

The WO$_3$ porous films were characterized in view of their crystallographic features and chemical composition by XRD and XPS. Data are compiled in Figs. 2 and 3, respectively.

Fig. 2a shows the XRD patterns of as-formed and annealed anodic WO$_3$ layers. In line with previous reports [42], the as-formed oxide film is amorphous and only reflections of the W metal substrate can be seen, peaking at 2θ = 40.3° and 73.2°, corresponding to the (110) and (211) crystallographic planes of cubic W, respectively [52].

The structures were converted into crystalline WO$_3$ by annealing in air at 450 °C (1 h). The XRD patterns of annealed anodic layers show characteristic reflections peaking at 2θ = 23.2°, 23.7° and 24.3° corresponding to the (002), (020) and (200) crystallographic planes of monoclinic WO$_3$, respectively [53]. For a WO$_3$ specimen composed of randomly oriented monoclinic crystallites, the relative intensity of the (002), (020) and (200) reflections is ∼1:1:1, that is, the peaks typically show virtually the same relative intensity. It can be noticed from the XRD patterns in Fig. 2b that with increasing the anodization time (1, 2 and 4 h), there is a change in the relative intensity of the peaks associated to the (002), (020) and (200) crystallographic planes. The reason for this may be a preferential growth of the monoclinic WO$_3$ crystals
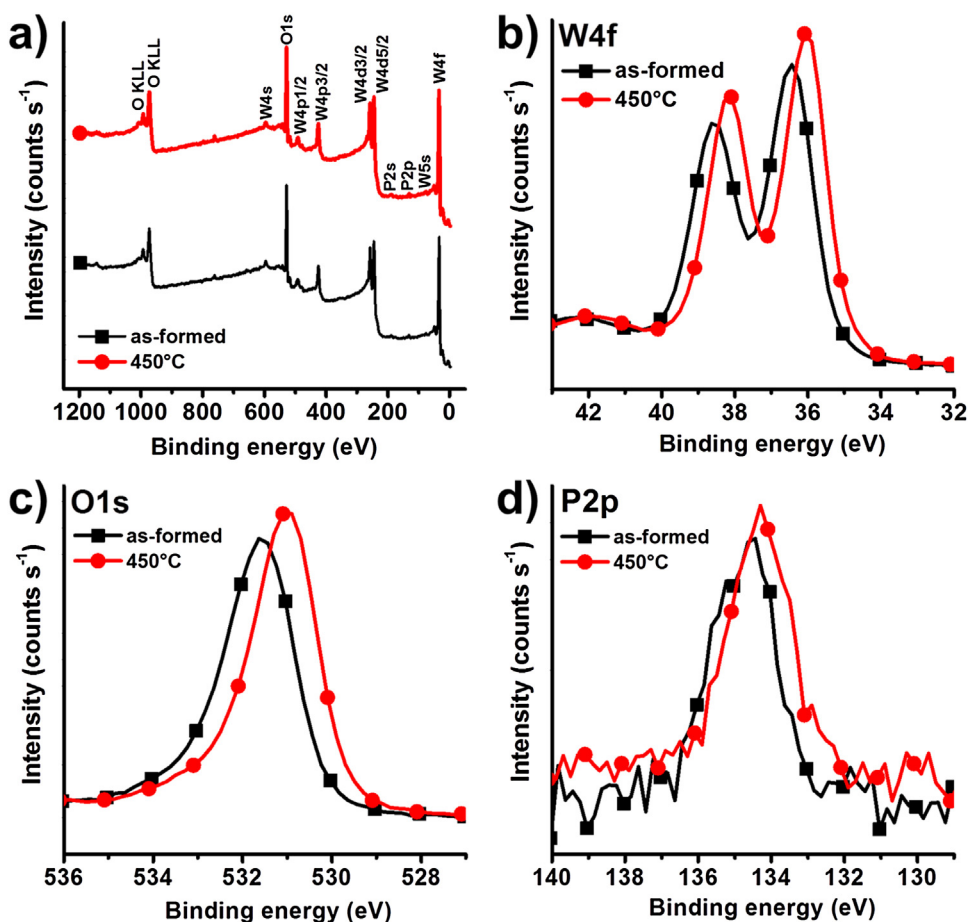
Fig. 3. XPS data of as-formed and annealed (450 °C, 1 h, air) WO$_3$ nanochannel layers grown by 2 h-long anodization experiments: (a) survey; (b-d) high resolution *spectra* measured in the (b) W4f, (c) O1 s and (d) P2p regions.

along the (002) and (020) planes − in other words, the longer the anodization time, the more intense the (002) and (020) reflections compared to the (200) peak.

The XPS survey (Fig. 3a) shows the as-formed and annealed anodic nanochannel layers are composed of only W and O, with small amounts of phosphorus (uptake from the electrolyte, discussed below) and adventitious carbon.

The high-resolution XPS *spectra* in the W 4f and O 1s regions are shown in Fig. 3b and c, respectively. For the annealed structures, the W4f 5/2 and 7/2 signals peak at 38.2 and 36.1 eV, respectively, with ΔB.E. ∼2.1 eV. Also, the O 1s signal peaks at 531.0 eV.

Table 1 summarizes the chemical composition of amorphous and crystalline layers determined from the XPS data. One can notice that in any case P is present at the surface of the WO$_3$ structures. Additionally, the W to O ratio is ∼1:3.2, which is slightly higher than expected for stoichiometric WO$_3$ (*i.e.*, 1:3), and the P2p XPS signal (HR *spectra* in Fig. 3d) peaks at 134.3 eV. Thus one can more likely conclude that PO$_4^{3-}$ species are adsorbed at the surface of the WO$_3$ nanochannels. This would be in line with the higher W

to O ratio, and also with the fact that the W 4f and O 1s signals are slightly shifted towards higher B.E. compared to data reported in the literature [54,55].

The HR-XPS *spectra* in Fig. 3b and c show also that the W 4f and O 1s signals of the crystalline layers are shifted towards slightly lower B.E. (*e.g.*, by ∼0.3–0.6 eV) compared to the as-formed structures − this is in line with previous reports [56], and is more probably ascribed to desorption of species (*e.g.*, C- and P-species − see Table 1) from the surface of the WO$_3$ nanochannels.

The electrochemical behaviour of all anodized WO$_3$ samples was investigated by cyclic voltammetry and galvanostatic charge-discharge measurements (performed in 1 M Na$_2$SO$_4$ solution). Fig. 4a shows a comparison of the cyclic voltammetry (CV) curves of various WO$_3$ layers (anodization time of 1, 2 and 4 h, annealing at 450° C) taken at a scan rate of 10 mV s^{-1}. The maximum current response was recorded for layers anodized for 2 h (Fig. 4a). The results of the galvanostatic charge-discharge measurements taken at current density of 2 A cm^{-3} (Fig. 4b) are in agreement with this finding, indicating a better redox capacitive behaviour of the 2 h anodized sample in comparison to the counterparts anodized for 1 or 4 h. Moreover, the plateau observed for all samples in the charge/discharge profiles (Fig. 4b) indicates that charge is also stored *via* redox processes, which should be occurring throughout the active nanochannels. These results are in accordance with the voltammetric waves observed in the CV plots.

The higher capacity obtained for the WO$_3$ structures grown for 2 h in contrast to those grown for 1 h is more likely ascribed to the larger surface area of the former. The *suboptimum* performance of 1 h anodized samples compared to thicker oxide films could be also

Table 1
W, O, P and C composition determined by XPS analysis of as-formed and annealed (450 °C, 1 h, air) WO$_3$ nanochannel layers grown by 2 h-long anodization experiments.

Sample	Atomic concentration (at%)				W:O ratio
	W4f	O1s	P2p	C1s	
2 h − as-formed	22.8	72.0	3.8	1.4	1:3.2
2 h − 450 °C	22.9	73.1	2.8	1.2	1:3.2

attributed to their poor mechanical properties, *i.e.*, short WO_3 nanochannels were found to be loosely attached to the W metal substrate and partly detached during electrochemical measurements. On the other hand, the 4 h anodized nanochannels are significantly thicker than those grown for 2 h ($\sim$800 *vs.* 400 nm), and this structure may lead to limited electrolyte permeation and

ion diffusion deep through the whole WO_3 layer, which could explain their decreased capacitance compared to the channels grown for 2 h.

Further electrochemical investigation was performed on the 2 h anodized sample, as shown in Fig. 4c and d. The CV curves (Fig. 4c) display clear oxidation peaks at −0.06 V and −0.3 V and a broad
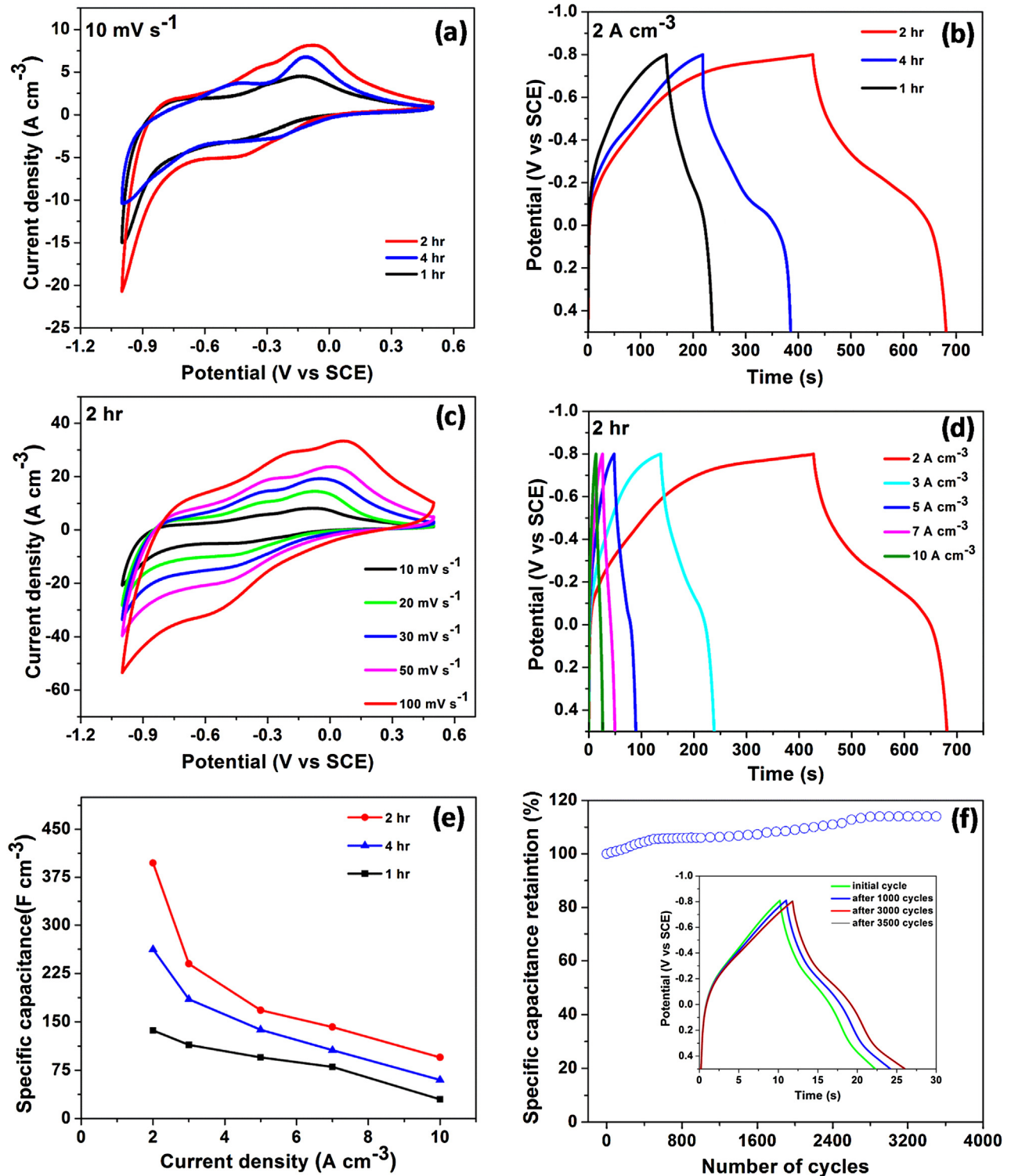
Fig. 4. (a) CV comparison plots of WO_3 (anodization time = 1 h, 2 h, and 4 h) at 10 mV s^{-1}; (b) Galvanostatic charge discharge comparison plot at 2 A cm^{-3}; (c–d) CV and galvanostatic charge discharge plot of 2 hr anodized sample at different scan rates and current densities, respectively (e) specific capacitance *vs.* current densities for all the samples (f) capacitance retention up to 3500 cycles at 10 A cm^{-3} (inset: charge discharge plots over time). All the experiments were performed with annealed sample (450 °C, air, 1 h).

reduction peak at -0.45 V. This redox response can be associated with the intercalation/de-intercalation of a quantity (x) of positive ions to balance an equal quantity of electrons (e^-) according to the following reaction [6,57]:

$$WO_3 + xH^+ + yNa^+ + (x+y)e^- \leftrightarrow H_xNa_yWO_3; 0 \leq (x+y) \leq 1 \quad (1)$$
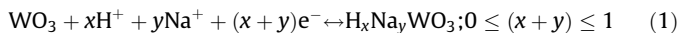
The ($x+y$) can vary from 0 to 1. The peak current response increases with increasing the scan rate, suggesting that the WO_3 nanochanneled architecture supported fast charge transfer and cation diffusion. Also, a shift in the oxidation and reduction peaks can be noticed when increasing the scan rate, and this shift is associated to polarization effects of the electrodes at higher scan rates. Moreover, symmetric oxidation and reduction peaks were retained even at high scan rates, this proving the reliability of the material when operated at fast rates.

The specific volumetric capacitance (C_s) of all the electrodes was calculated from the galvanostatic discharge curves (Fig. 4b) data using equation:

$$C_s = \frac{I\Delta t}{\Delta V} \quad (2)$$

where, C_s is the volumetric specific capacitance ($F\,cm^{-3}$), I is the current density ($A\,cm^{-3}$, considering a volume of the electrode material calculated by multiplying the height of the nanochannels obtained from SEM analysis to the nominal electrode area, i.e. $\sim 2\,cm^2$), ΔV is the potential window, and Δt is the discharge time (s). The specific capacitance value obtained for 2 h anodized sample is $397\,F\,cm^{-3}$ at $2\,A\,cm^{-3}$, which is significantly higher

compared to $262\,F\,cm^{-3}$ and $136\,F\,cm^{-3}$ obtained for 4 h and 1 h anodized samples, respectively.

The specific capacitance values at different current density ranging from $2-10\,A\,cm^{-3}$ are depicted in Fig. 4e. The best performing sample (anodized for 2 h) showed at a current density of $10\,A\,cm^{-3}$ a specific volumetric capacitance of ca. $110\,F\,cm^{-3}$, that is $\sim 28\%$ of that measured at $2\,A\,cm^{-3}$. This volumetric capacitance, measured at a relatively high current density ($10\,A\,cm^{-3}$), is comparable to data reported in the literature (see e.g. refs [17,19]).

In general, the 2 h anodized material showed remarkable redox capacitive response (in neutral 1 M Na_2SO_4 aqueous solutions) in comparison to WO_3 electrodes previously reported in the literature, primarily in the negative potential range. For example, Peng et al. reported WO_3 nanorods active in the negative potential range ($-0.7-0.2$ V) which deliver specific capacitance values of $385\,F\,g^{-1}$ at $1\,A\,g^{-1}$ in 1 M H_2SO_4 [19]. Shinde and co-workers reported on WO_3 thin films synthesized by Silar technique and obtained specific capacitance of $266\,F\,g^{-1}$ at $10\,mV\,s^{-1}$ measured in potential window $-0.7-0.4$ V in 1 M Na_2SO_4 solution [17]. Gao et al. reported WO_3 nanowires grown on carbon cloth having specific capacitance of $521\,F\,g^{-1}$ at $1\,A\,g^{-1}$ ($-0.6-0.3$ V) in 2 M H_2SO_4 solution [23]. Other works reported specific capacitances of $290\,F\,g^{-1}$ at $25\,mV\,s^{-1}$ ($-0.6-0.2$ V) in 0.5 M H_2SO_4 solution [16], and of $639.8\,F\,g^{-1}$ at $10\,mV\,s^{-1}$ ($-0.6-0$ V) in 1 M H_2SO_4 electrolyte [21].

For a more direct comparison, our results (that were measured in a neutral electrolyte and without using any additive) can be also
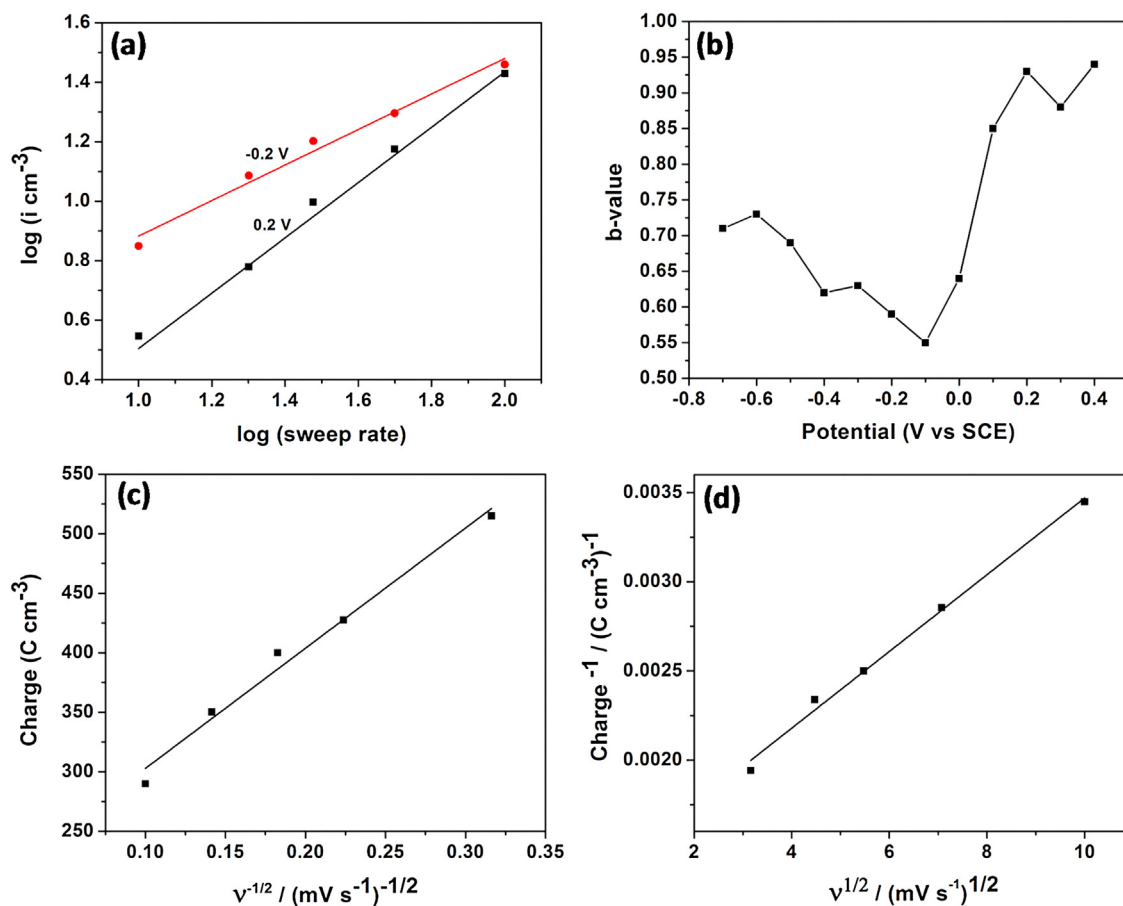

Fig. 5. Kinetic analysis of the 2 h anodized film; (a) the power law dependence of current i vs. the sweep rate shows good linearity. The two curves correspond to -0.2 V, $b = 0.59$ and 0.2 V, $b = 0.93$, respectively (b) b-values as a function of potential for anodic current for varying sweep rate; relationship of (c) charge Q vs. $V^{-1/2}$ and (d) Q^{-1} vs. $V^{1/2}$.

compared to volumetric capacitance data reported in the literature (*i.e.*, in terms of F cm^{-3}). Values in the range of $\sim$40–340 F cm^{-3} are reported for various composite WO$_3$ electrodes [58–61], while a volumetric capacitance of $\sim$640 F cm^{-3} is reported by Yoon et al. for m-WO$_{3-x}$ electrodes used in acidic electrolytes [62]. Worth noting, results reported for WO$_3$ electrodes are mostly measured in acidic *media*. Under these experimental conditions tungsten oxide may also behave as electrocatalyst for hydrogen generation–as a result, the material working potential window should be narrowed [63,64], which would consequently lead to a limited performance of the electrode in terms of lower energy density.

On the contrary, the WO$_3$ nanochannel layers are explored in this work in a neutral electrolyte, *i.e.* aqueous 1 M Na$_2$SO$_4$, and this widens the material working potential window from -0.8 to 0.5 V. The widening of the working potential window results in the enhancement of the overall energy density when using these electrodes in an asymmetric configuration.

Furthermore, the improved capacitive behaviour can also be a consequence of a relatively high intrinsic electronic conductivity of the material, provided by the interconnected structure.

In order to evaluate the stability of the material, long term charge-discharge experiments were carried out. Galvanostatic charge-discharge measurements were performed at 10 A cm^{-3}. The results in Fig. 4f show remarkable capacitance retain up to 3500 charge-discharge cycles. More precisely, a slight increase in the capacitance was observed that could be ascribed to an increased accessibility/diffusion of ions deep into the nanochannel structure after several cycles, as a consequence of a longer soaking time (similar results can be found in the literature [59,61,65]). The capacitance was observed to increase up to 114% of the initial capacitance in the first 3000 cycles. Afterwards, the measured capacitance stabilized and became constant (up to 3500 cycles), as shown from the charge-discharge plot in the inset of Fig. 4f. More generally, the 2 h anodized structures resulted mechanically stable (showed good adhesion to the substrate) and their remarkable capacitance retain can be ascribed to the 1D nanochannel structure that can accommodate strain and sustain repeated volume changes [30–32,66].

The charge storage mechanism was also studied for the best performing sample (2 h anodized structure). It is known that the

overall capacitance of a material can be also ascribed to other *phenomena* such as surface double layer formation or surface faradaic adsorption, and to bulk faradaic intercalation/de-intercalation reactions. The occurrence of these different mechanisms of energy storage can be identified (and differentiated from the others) by analysing the CV data at various sweep rates according to equation (3), and can be illustrated by plotting log (*i*) *vs.* log (V) as a function of potential [67,68]:

$$i = a\ V^b \tag{3}$$

According to equation (3), the measured current *i* obeys to a power law function of the sweep rate V. Both *a* and *b* are variable parameters. When *b* is close to 1, the current response is predominantly capacitive in nature. On the other hand, the current flow at any given potential is expected to vary with the square root of the scan rate for the diffusion controlled process and in this case *b* equals to 0.5.

In order to determine the *b* values, log *i* was plotted versus log V for different potentials. According to equation (3) this representation gives rise to a straight line with a slope equals to *b*. As an example, plots of log *i* versus log V at applied potentials of -0.2 V and 0.2 V are illustrated in Fig. 5a, showing a nearly linear behaviour and presenting distinct *b*-values of 0.59 and 0.93 respectively. In Fig. 5b, the *b*-values are shown as a function of different applied potentials. In the positive potential range (0.1–0.4 V) the *b*-values approach 1 indicating that the current response arises predominantly either from redox *phenomena* at the nanochannel surface or from double layer formation. However, in the negative potential region, *b*-values are in the range of 0.55 to 0.7 indicating the occurrence of diffusion controlled processes, which can be associated with diffusion of cations towards the bulk of the material [68].

After observing the presence of diffusion controlled process in the charge storage behaviour of WO$_3$ nanochanneled films, we further studied and separated the contributions of surface capacitance and diffusion-controlled insertion from the total charge storage, using an approach reported elsewhere [28,69]. In this model, the relationship between charge (Q [coulomb]) and the scan rate of the cyclic voltammogram is described by the Eqs. (4) and (5) [69]:
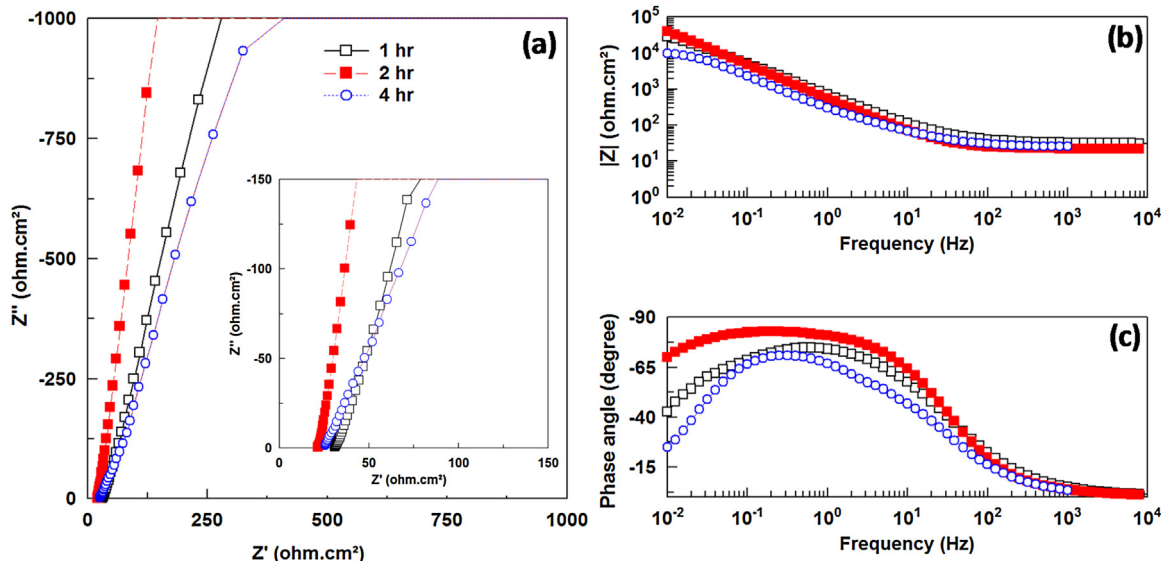

Fig. 6. (a) Nyquist plot (inset: magnified view) and (b-c) Bode plot obtained from electrochemical impedance spectroscopy (EIS) measurements of crystalline anodic WO$_3$ layers.

$$Q = Q_{V=\infty} + \text{constant } (V^{-1/2}) \tag{4}$$

$$Q^{-1} = Q^{-1}_{V=0} + \text{constant } (V^{1/2}) \tag{5}$$

where $Q_{V=\infty}$ is the surface adsorption charge, corresponding to the voltammetric charge at $V = \infty$ and $Q_{V=0}$ is the total charge, which is the value at $V = 0$. Therefore, by plotting Q versus $V^{-1/2}$ and Q^{-1} versus $V^{1/2}$ the surface adsorbed double layer capacitance and the total capacitance can be determined from the y-axis intercepts (Fig. 5c and d). After calculations, the results revealed that the contribution from the double layer capacitance and surface adsorption is about ~27% and the remaining capacitance (~73%) arises from the diffusion-controlled redox processes.

To further study the electrochemical behaviour, electrochemical impedance spectroscopy (EIS) experiments were performed for all the anodized and annealed samples at the open circuit potential.

Fig. 6a shows the Nyquist plot for the WO$_3$ films anodized for 1, 2 and 4 h. From the intercept of the plot with the real axis in the high frequency region (inset in Fig. 6a) it is possible to assess the equivalent series resistance (sum of contact resistance, electrolyte resistance and material resistance). It can be clearly observed that the electrode anodised for 2 h presents the lowest equivalent resistance, which can be associated with its highly-ordered morphology contributing to a beneficial intrinsic electronic conductivity.

On the other hand, the low frequency region is characterized by the presence of straight lines which present lower slopes in the case of the oxide films prepared by 1 and 4 h-long anodization. This fact can be associated with the development of Warburg behaviour associated with the occurrence of diffusion-controlled processes. This is particularly in good agreement with the morphological features of films anodized for 4 h, the structure of which may lead to limited electrolyte permeation and ion diffusion into the thick WO$_3$ structure. This can also be noticed in the Bode plot (Fig. 6c), where the 2 h anodized sample reveals at medium-low frequency a higher phase angle approaching $-90°$, which indicates a more pronounced capacitive response. These results, which highlight the enhanced capacitive behaviour of the 4 h anodized layers, are in good agreement with the cyclic voltammetry and charge discharge comparison curves shown in Fig. 4a and b.

4. Conclusion

The pseudocapacitive behaviour of anodically grown WO$_3$ nanochannel layers was explored and the electrochemical results proved that these structures are promising materials for fabricating anodes for asymmetric supercapacitors. Layers grown by 2 h-long anodization displayed superior volumetric capacitance compared to layers anodized either for shorter or longer times (397 F cm^{-3} at 2 A cm^{-3} in a relatively wide potential range of 1.3 V). The material exhibited full specific capacitance retain over 3500 charge-discharge cycles at 10 A cm^{-3}. The WO$_3$ structures were investigated with a focus on mechanistic aspects related to charge storage dynamic. The b-values obtained at different potentials allowed to distinguish the contribution to the overall capacitance of the nanochannel architecture ascribed to surface or bulk effects. Further analysis revealed that 27% of the total capacitance is from surface adsorption/desorption process, whereas the remaining 73% results from a diffusion-controlled process. The promising capacitance and capacitance retention results can be associated to the nanochannel architecture, which offers large specific surface area, short charge transport pathways, low intrinsic resistance, and long-lasting mechanical robustness allowing strain accommodation during intercalation/deintercalation processes.

References

[1] S. Wang, L. Pan, J.-J. Song, W. Mi, J.-J. Zou, L. Wang, X. Zhang, Titanium-Defected Undoped Anatase TiO$_2$ with p-Type Conductivity, Room-Temperature Ferromagnetism, and Remarkable Photocatalytic Performance, Journal of the American Chemical Society 137 (2015) 2975–2983.
[2] F. Bonaccorso, L. Colombo, G. Yu, M. Stoller, V. Tozzini, A.C. Ferrari, R.S. Ruoff, V. Pellegrini, Graphene, related two-dimensional crystals, and hybrid systems for energy conversion and storage, Science 347 (2015).
[3] X. Wang, L. Sun, R. Agung Susantyoko, Y. Fan, Q. Zhang, Ultrahigh volumetric capacity lithium ion battery anodes with CNT–Si film, Nano Energy 8 (2014) 71–77.
[4] Y. Wang, T. Wang, P. Da, M. Xu, H. Wu, G. Zheng, Silicon Nanowires for Biosensing, Energy Storage, and Conversion, Advanced Materials 25 (2013) 5177–5195.
[5] P. Zhang, J. Zhang, J. Gong, Tantalum-based semiconductors for solar water splitting, Chemical Society Reviews 43 (2014) 4395–4422.
[6] P. Simon, Y. Gogotsi, Materials for electrochemical capacitors, Nat Mater 7 (2008) 845–854.
[7] B.E. Conway, Electrochemical supercapacitors: scientific fundamentals and technological applications, Springer Science & Business Media, 2013.
[8] J.M. Miller, B. Dunn, T.D. Tran, R.W. Pekala, Deposition of Ruthenium Nanoparticles on Carbon Aerogels for High Energy Density Supercapacitor Electrodes, Journal of The Electrochemical Society 144 (1997) L309–L311.
[9] A. Lewandowski, M. Galinski, Practical and theoretical limits for electrochemical double-layer capacitors, Journal of Power Sources 173 (2007) 822–828.
[10] G. Wang, L. Zhang, J. Zhang, A review of electrode materials for electrochemical supercapacitors, Chemical Society Reviews 41 (2012) 797–828.
[11] B. Akinwolemiwa, C. Peng, G.Z. Chen, Redox Electrolytes in Supercapacitors, Journal of The Electrochemical Society 162 (2015) A5054–A5059.
[12] M. Yu, Z. Wang, Y. Han, Y. Tong, X. Lu, S. Yang, Recent progress in the development of anodes for asymmetric supercapacitors, Journal of Materials Chemistry A 4 (2016) 4634–4658.
[13] B. Yin, S. Zhang, H. Jiang, F. Qu, X. Wu, Phase-controlled synthesis of polymorphic MnO$_2$ structures for electrochemical energy storage, Journal of Materials Chemistry A 3 (2015) 5722–5729.
[14] Y. Jiao, Y. Liu, B. Yin, S. Zhang, F. Qu, X. Wu, Hybrid α-Fe$_2$O$_3$@NiO heterostructures for flexible and high performance supercapacitor electrodes and visible light driven photocatalysts, Nano Energy 10 (2014) 90–98.
[15] X. Wu, Z. Han, X. Zheng, S. Yao, X. Yang, T. Zhai, Core-shell structured Co$_3$O$_4$@NiCo$_2$O$_4$ electrodes grown on flexible carbon fibers with superior electrochemical properties, Nano Energy 31 (2017) 410–417.
[16] K.-H. Chang, C.-C. Hu, C.-M. Huang, Y.-L. Liu, C.-I. Chang, Microwave-assisted hydrothermal synthesis of crystalline WO$_3$–WO$_3$·0.5H$_2$O mixtures for pseudocapacitors of the asymmetric type, Journal of Power Sources 196 (2011) 2387–2392.
[17] N.M. Shinde, A.D. Jagadale, V.S. Kumbhar, T.R. Rana, J. Kim, C.D. Lokhande, Wet chemical synthesis of WO$_3$ thin films for supercapacitor application, Korean Journal of Chemical Engineering 32 (2015) 974–979.
[18] X. Xiao, T. Ding, L. Yuan, Y. Shen, Q. Zhong, X. Zhang, Y. Cao, B. Hu, T. Zhai, L. Gong, J. Chen, Y. Tong, J. Zhou, Z.L. Wang, WO$_{3-x}$/MoO$_{3-x}$ Core/Shell Nanowires on Carbon Fabric as an Anode for All-Solid-State Asymmetric Supercapacitors, Advanced Energy Materials 2 (2012) 1328–1332.
[19] H. Peng, G. Ma, K. Sun, J. Mu, M. Luo, Z. Lei, High-performance aqueous asymmetric supercapacitor based on carbon nanofibers network and tungsten trioxide nanorod bundles electrodes, Electrochimica Acta 147 (2014) 54–61.
[20] P. Yang, P. Sun, L. Du, Z. Liang, W. Xie, X. Cai, L. Huang, S. Tan, W. Mai, Quantitative Analysis of Charge Storage Process of Tungsten Oxide that

Combines Pseudocapacitive and Electrochromic Properties, The Journal of Physical Chemistry C 119 (2015) 16483–16489.

[21] P. Yang, P. Sun, Z. Chai, L. Huang, X. Cai, S. Tan, J. Song, W. Mai, Large-Scale Fabrication of Pseudocapacitive Glass Windows that Combine Electrochromism and Energy Storage, Angewandte Chemie 126 (2014) 12129–12133.

[22] F. Wang, X. Zhan, Z. Cheng, Z. Wang, Q. Wang, K. Xu, M. Safdar, J. He, Tungsten Oxide@Polypyrrole Core–Shell Nanowire Arrays as Novel Negative Electrodes for Asymmetric Supercapacitors, Small 11 (2015) 749–755.

[23] L. Gao, X. Wang, Z. Xie, W. Song, L. Wang, X. Wu, F. Qu, D. Chen, G. Shen, High-performance energy-storage devices based on WO$_3$ nanowire arrays/carbon cloth integrated electrodes, Journal of Materials Chemistry A 1 (2013) 7167–7173.

[24] H. Zheng, J.Z. Ou, M.S. Strano, R.B. Kaner, A. Mitchell, K. Kalantar-zadeh, Nanostructured Tungsten Oxide-Properties, Synthesis, and Applications, Advanced Functional Materials 21 (2011) 2175–2196.

[25] C. Di Valentin, G. Pacchioni, Spectroscopic Properties of Doped and Defective Semiconducting Oxides from Hybrid Density Functional Calculations, Accounts of Chemical Research 47 (2014) 3233–3241.

[26] S.K. Deb, Opportunities and challenges in science and technology of WO$_3$ for electrochromic and related applications, Solar Energy Materials and Solar Cells 92 (2008) 245–258.

[27] D. Wang, J. Li, X. Cao, G. Pang, S. Feng, Hexagonal mesocrystals formed by ultra-thin tungsten oxide nanowires and their electrochemical behaviour, Chemical Communications 46 (2010) 7718–7720.

[28] T. Nguyen, M. Boudard, L. Rapenne, M.J. Carmezim, M.F. Montemor, Morphological changes and electrochemical response of mixed nickel manganese oxides as charge storage electrodes, Journal of Materials Chemistry A 3 (2015) 10875–10882.

[29] T. Nguyen, M. Boudard, L. Rapenne, O. Chaix-Pluchery, M.J. Carmezim, M.F. Montemor, Structural evolution, magnetic properties and electrochemical response of MnCo$_2$O$_4$ nanosheet films, RSC Advances 5 (2015) 27844–27852.

[30] L. Yang, S. Cheng, Y. Ding, X. Zhu, Z.L. Wang, M. Liu, Hierarchical Network Architectures of Carbon Fiber Paper Supported Cobalt Oxide Nanonet for High-Capacity Pseudocapacitors, Nano Letters 12 (2012) 321–325.

[31] C.K. Chan, H. Peng, G. Liu, K. McIlwrath, X.F. Zhang, R.A. Huggins, Y. Cui, High-performance lithium battery anodes using silicon nanowires, Nat Nano 3 (2008) 31–35.

[32] J. Jiang, Y. Li, J. Liu, X. Huang, C. Yuan, X.W. Lou, Recent Advances in Metal Oxide-based Electrode Architecture Design for Electrochemical Energy Storage, Advanced Materials 24 (2012) 5166–5180.

[33] H. Masuda, K. Fukuda, Ordered Metal Nanohole Arrays Made by a Two-Step Replication of Honeycomb Structures of Anodic Alumina, Science 268 (1995) 1466–1468.

[34] M. Assefpour-Dezfuly, C. Vlachos, E.H. Andrews, Oxide morphology and adhesive bonding on titanium surfaces, Journal of Materials Science 19 (1984) 3626–3639.

[35] V. Zwilling, M. Aucouturier, E. Darque-Ceretti, Anodic oxidation of titanium and TA6 V alloy in chromic media. An electrochemical approach, Electrochimica Acta 45 (1999) 921–929.

[36] A. Ghicov, P. Schmuki, Self-ordering electrochemistry: a review on growth and functionality of TiO2nanotubes and other self-aligned MO$_x$ structures, Chemical Communications (2009) 2791–2808.

[37] D. Kowalski, D. Kim, P. Schmuki, TiO$_2$ nanotubes, nanochannels and mesosponge: Self-organized formation and applications, Nano Today 8 (2013) 235–264.

[38] P. Roy, S. Berger, P. Schmuki, TiO$_2$ Nanotubes: Synthesis and Applications, Angewandte Chemie International Edition 50 (2011) 2904–2939.

[39] K. Lee, A. Mazare, P. Schmuki, One-Dimensional Titanium Dioxide Nanomaterials: Nanotubes, Chemical Reviews 114 (2014) 9385–9454.

[40] B.-X. Zou, Y. Liang, X.-X. Liu, D. Diamond, K.-T. Lau, Electrodeposition and pseudocapacitive properties of tungsten oxide/polyaniline composite, Journal of Power Sources 196 (2011) 4842–4848.

[41] H. Wei, X. Yan, S. Wu, Z. Luo, S. Wei, Z. Guo, Electropolymerized Polyaniline Stabilized Tungsten Oxide Nanocomposite Films: Electrochromic Behavior and Electrochemical Energy Storage, The Journal of Physical Chemistry C 116 (2012) 25052–25064.

[42] M. Altomare, O. Pfoch, A. Tighineanu, R. Kirchgeorg, K. Lee, E. Selli, P. Schmuki, Molten o-H$_3$PO$_4$: A New Electrolyte for the Anodic Synthesis of Self-Organized Oxide Structures-WO$_3$ Nanochannel Layers and Others, Journal of the American Chemical Society 137 (2015) 5646–5649.

[43] J.E. Houser, K.R. Hebert, The role of viscous flow of oxide in the growth of self-ordered porous anodic films, Nat Mater 8 (2009) 415–420.

[44] K.R. Hebert, S.P. Albu, I. Paramasivam, P. Schmuki, Morphological instability leading to formation of porous anodic oxide films, Nat Mater 11 (2012) 162–166.

[45] X. Zhou, N.T. Nguyen, S. Özkan, P. Schmuki, Anodic TiO$_2$ nanotube layers: Why does self-organized growth occur—A mini review, Electrochemistry Communications 46 (2014) 157–162.

[46] N. Mukherjee, M. Paulose, O.K. Varghese, G.K. Mor, C.A. Grimes, Fabrication of nanoporous tungsten oxide by galvanostatic anodization, Journal of Materials Research 18 (2003) 2296–2299.

[47] H. Tsuchiya, J.M. Macak, I. Sieber, L. Taveira, A. Ghicov, K. Sirotna, P. Schmuki, Self-organized porous WO$_3$ formed in NaF electrolytes, Electrochemistry Communications 7 (2005) 295–298.

[48] S. Berger, H. Tsuchiya, A. Ghicov, P. Schmuki, High photocurrent conversion efficiency in self-organized porous WO$_3$, Applied Physics Letters 88 (2006) 203119.

[49] L. Hu, J.W. Choi, Y. Yang, S. Jeong, F. La Mantia, L.-F. Cui, Y. Cui, Highly conductive paper for energy-storage devices, Proceedings of the National Academy of Sciences 106 (2009) 21490–21494.

[50] M.D. Stoller, R.S. Ruoff, Best practice methods for determining an electrode material's performance for ultracapacitors, Energy & Environmental Science 3 (2010) 1294–1301.

[51] F. Riboni, N.T. Nguyen, S. So, P. Schmuki, Aligned metal oxide nanotube arrays: key-aspects of anodic TiO$_2$ nanotube formation and properties, Nanoscale Horizons 1 (2016) 445–466.

[52] M.E. Straumanis, Absorption Correction in Precision Determination of Lattice Parameters, Journal of Applied Physics 30 (1959) 1965–1969.

[53] B. Loopstra, H. Rietveld, Further refinement of the structure of WO$_3$, Acta Crystallographica Section B: Structural Crystallography and Crystal Chemistry 25 (1969) 1420–1421.

[54] T.L. Barr, An ESCA study of the termination of the passivation of elemental metals, The Journal of Physical Chemistry 82 (1978) 1801–1810.

[55] V.I. Nefedov, M.N. Firsov, I.S. Shaplygin, Electronic structures of MRhO$_2$, MRh$_2$O$_4$ RhMO$_4$ and Rh$_2$MO$_6$ on the basis of X-ray spectroscopy and ESCA data, Journal of Electron Spectroscopy and Related Phenomena 26 (1982) 65–78.

[56] T.G.G. Maffeis, D. Yung, L. LePennec, M.W. Penny, R.J. Cobley, E. Comini, G. Sberveglieri, S.P. Wilks, STM and XPS characterisation of vacuum annealed nanocrystalline WO$_3$ films, Surface Science 601 (2007) 4953–4957.

[57] Z.-F. Huang, J. Song, L. Pan, X. Zhang, L. Wang, J.-J. Zou, Tungsten Oxides for Photocatalysis, Electrochemistry, and Phototherapy, Advanced Materials 27 (2015) 5309–5327.

[58] C. Jo, J. Hwang, H. Song, A.H. Dao, Y.-T. Kim, S.H. Lee, S.W. Hong, S. Yoon, J. Lee, Block-Copolymer-Assisted One-Pot Synthesis of Ordered Mesoporous WO$_{3-x}$/Carbon Nanocomposites as High-Rate-Performance Electrodes for Pseudocapacitors, Advanced Functional Materials 23 (2013) 3747–3754.

[59] Y. Zhou, S. Ko, C.W. Lee, S.G. Pyo, S.-K. Kim, S. Yoon, Enhanced charge storage by optimization of pore structure in nanocomposite between ordered mesoporous carbon and nanosized WO$_{3-x}$, Journal of Power Sources 244 (2013) 777–782.

[60] X. Huang, H. Liu, X. Zhang, H. Jiang, High Performance All-Solid-State Flexible Micro-Pseudocapacitor Based on Hierarchically Nanostructured Tungsten Trioxide Composite, ACS Applied Materials & Interfaces 7 (2015) 27845–27852.

[61] C.-C. Huang, W. Xing, S.-P. Zhuo, Capacitive performances of amorphous tungsten oxide prepared by microwave irradiation, Scripta Materialia 61 (2009) 985–987.

[62] S. Yoon, E. Kang, J.K. Kim, C.W. Lee, J. Lee, Development of high-performance supercapacitor electrodes using novel ordered mesoporous tungsten oxide materials with high electrical conductivity, Chemical Communications 47 (2011) 1021–1023.

[63] A. Phuruangrat, D.J. Ham, S.J. Hong, S. Thongtem, J.S. Lee, Synthesis of hexagonal WO$_3$ nanowires by microwave-assisted hydrothermal method and their electrocatalytic activities for hydrogen evolution reaction, Journal of Materials Chemistry 20 (2010) 1683–1690.

[64] R. Ganesan, J.S. Lee, An electrocatalyst for methanol oxidation based on tungsten trioxide microspheres and platinum, Journal of Power Sources 157 (2006) 217–221.

[65] K.K. Upadhyay, S. Eugénio, R. Della Noce, T.M. Silva, M.J. Carmezim, M.F. Montemor, Hydrothermally grown Ni$_{0.7}$Zn$_{0.3}$O directly on carbon fiber paper substrate as an electrode material for energy storage applications, International Journal of Hydrogen Energy 41 (2016) 9876–9884.

[66] G. Zhang, X.W. Lou, Controlled Growth of NiCo$_2$O$_4$ Nanorods and Ultrathin Nanosheets on Carbon Nanofibers for High-performance Supercapacitors, Scientific Reports 3 (2013) 1470.

[67] H. Lindström, S. Södergren, A. Solbrand, H. Rensmo, J. Hjelm, A. Hagfeldt, S.-E. Lindquist, Li$^+$ Ion Insertion in TiO$_2$ (Anatase). 1. Chronoamperometry on CVD Films and Nanoporous Films, The Journal of Physical Chemistry B 101 (1997) 7710–7716.

[68] M. Sathiya, A.S. Prakash, K. Ramesha, J.M. Tarascon, A.K. Shukla, V$_2$O$_5$-Anchored Carbon Nanotubes for Enhanced Electrochemical Energy Storage, Journal of the American Chemical Society 133 (2011) 16291–16299.

[69] S. Ardizzone, G. Fregonara, S. Trasatti, "Inner" and "outer" active surface of RuO$_2$ electrodes, Electrochimica Acta 35 (1990) 263–267.